Volume 1 | Number 1 | Jan 2013 | Pages 1–100

CrystEngComm

www.rsc.org/crystengcomm

ROYAL SOCIETY OF CHEMISTRY

ROYAL SOCIETY OF CHEMISTRY

www.rsc.org/crystengcomm

CrystEngComm

ARTICLE

Influence of Ta^{5+} content on the crystallographic structure and electrical properties of [001]$_{PC}$-oriented (Li,Na,K)(Nb,Ta)O$_3$ single crystals

Hairui Liu,*[a][b][c] Philippe Veber,[ab] Jurij Koruza,[c] Daniel Rytz,[d] Michael Josse,[ab] Jürgen Rödel[c] and Mario Maglione[ab]

A series of centimeter-sized lead-free piezoelectric Li$^+$-, Ta^{5+}-modified (Na,K)NbO$_3$ single crystals with ABO$_3$ perovskite structure was successfully grown by the top-seeded solution growth method. Effective segregation of the elements was considered in order to further develop the growth of Li$^+$-, Ta^{5+}-modified (Na,K)NbO$_3$ single crystals. Crystallographic structure and electrical behaviour along the [001]$_{PC}$ orientation were studied. X-ray diffraction, Raman spectroscopy and dielectric studies reveal that the increase of Ta^{5+} content reduces the orthorhombic-tetragonal phase transition. Bipolar and unipolar strain curves were investigated at 2 kV·mm^{-1}. The highest bipolar and unipolar strains associated with a large-signal piezoelectric constant of 368 pm·V^{-1} were achieved for Li$_{0.02}$Na$_{0.626}$K$_{0.354}$Nb$_{0.808}$Ta$_{0.192}$O$_3$. The asymmetric bipolar strain curves were observed and related to the existence of internal bias fields induced by (V$_A'$-V$_O^{··}$)$^·$ defect dipoles, which were created during the crystal growth process.

1 Introduction

Lead-free piezoelectrics are currently studied and developed as alternatives to lead-based materials, such as Pb(Ti,Zr)O$_3$ (PZT), owing to environmental issues caused by the toxicity of lead.[1-3] At present time, Na$_{0.5}$Bi$_{0.5}$TiO$_3$-based,[1, 4, 5] BaTiO$_3$-based[6-8] and Na$_x$K$_{1-x}$NbO$_3$-based (KNN)[9, 10] lead-free piezoelectric materials exhibit the most promising properties, which could compete with those of PZT, as referenced by Saito *et al.* in 2004.[9] Since then, the KNN-based systems have attracted much attention, whereby enhanced dielectric, ferroelectric and piezoelectric properties could be obtained in the vicinity of their Polymorphic Phase Transition (PPT) between the orthorhombic and the tetragonal phases.[11-14] This phase transition, occurring in pure KNN at 200 °C, can be shifted to room temperature by chemical modifications, which is an effective way to improve electrical performance. Of particular significance are Li$^+$, Sb^{5+} and Ta^{5+} substitutions. For instance, a d$_{33}$ of about 230 pC·N^{-1} with a planar mode coupling coefficient k$_p$ = 0.51, and a relatively high Curie temperature T$_c$ = 323 ^{o}C were reported in polycrystalline (Li,Na,K)(Nb,Ta)O$_3$ (KNLTN) ceramic with 3 mol % Li$^+$ and 20 mol % Ta^{5+}, while even higher properties were reported in textured (Li,Na,K)(Nb,Ta,Sb)O$_3$ (KNLSTN) polycrystalline ceramics with d$_{33}$ = 416 pC·N^{-1} and a high planar mode coupling coefficient

k$_p$ = 0.61.[9, 15] At this point it should be noted that Sb is a toxic element and should therefore be avoided.

The research on perovskite lead-based piezoelectric materials revealed that single crystals exhibit much higher piezoelectric properties than polycrystalline ceramics, due to their anisotropic properties and the absence of intergranular interactions.[16] Recently, Huo *et al.*[17] have grown a Mn-doped [Li$_x$(Na$_{0.484}$K$_{0.516}$)$_{1-x}$](Nb$_{0.713}$Ta$_{0.287}$)O$_3$ single crystal with a piezoelectric coefficient d$_{33}$ = 630 pC·N^{-1} and a very high longitudinal mode coupling coefficient k$_{33}$ = 0.95. Nevertheless, the exact composition was not reported. In general, lithium content is hardly measured due to the chemical stability of KNN-based crystals which are poorly dissolvable in acid solutions used for Inductively Coupled Plasma Optical Emission Spectroscopy (ICP-OES) analysis and due to its low content which is difficult to detect in a precise manner. Table 1 summarizes selected properties of pure and modified-KNN single crystals grown by various techniques such as Top-Seeded Solution Growth (TSSG), floating zone method (FZM), flux-Bridgman and solid state crystal growth (SSCG). As evident, only a few Li$^+$ or/and Ta^{5+}-modified KNN-based single crystals with the orthorhombic-tetragonal phase transition temperature (T$_{O-T}$) close to the room temperature were reported. The highest measured room temperature dielectric permittivity ε$_r$ was 1015,[18] while most ε$_r$ values are lower than 800.

The KNN-based single crystal growth is affected by the difficulty in controlling stoichiometry of the crystals. On the one hand, the compositions of as-grown crystals are different from those of the initial liquid due to the thermodynamic segregation of the elements in KNN-based solid solutions.[19, 20] On the other hand, Prakasam *et al.*[21] noted that the segregation phenomena for individual elements

a. CNRS, ICMCB, UPR 9048, Pessac 33600, France
b. Université de Bordeaux, ICMCB, UPR 9048, Pessac 33600, France
c. Institute of Materials Science, Technische Universität Darmstadt, Alarich-Weiss-Straße 2, Darmstadt 64287, Germany. Email: liu@ceramics.tu-darmstadt.de
d. FEE GmbH, Struthstr. 2, Idar-Oberstein 55743, Germany

Table 1 Comparison of the properties of KNN-based single crystals

Composition	Method	T_{O-T} (°C)	T_c (°C)	ε_r (at RT)	d_{33} (pC·N^{-1})	d_{33}^* (pm·V^{-1})	Ref.
KNLTN	TSSG	-23	197				22
KNLTN:Mn	TSSG	30	235	350	630	870	17
KNLTN	TSSG	49	232	790	354	672	22
KNLTN	TSSG	79	276	500	255	470	23
KNTN	TSSG	120	298	267	162		24
KNTN	TSSG	120	290	300	~170		25
KNTN	FZM	171	370	128			26
KNTN^a	FZM			148	70		26
KNLN	Bridgman^b	179	421	530	161		27
KNLN	Bridgman	192	426	185	405		28
KNLN:Mn	Bridgman^b	186	441	614	190		27
KNLN:Mn	Bridgman^b	195	446	899			27
KNN	TSSG	180	400	423	70		29
KNN^a	TSSG	185	400	375	145		29
KNN^c	SSCG	192	410	1015		80	18
KNN	FZM	192	405	114	76		26
KNN^a	FZM			123	65		26

^{a}[110]$_{PC}$-oriented single crystals.

^{b}flux-Bridgman.

^{c}[1 $\bar{3}$ 1]$_O$-oriented single crystals.

in KNLSTN single crystals were also induced by the preferential volatilization of some elements from the liquid solution during the growth process occurring at high temperature.

In the present work, several growth experiments of KNLTN single crystals were undertaken by the TSSG method and the segregation phenomena of lithium and tantalum were examined. The influence of Ta^{5+} content on structural and electrical properties is investigated and electric-field-induced bipolar strain curves of KNLTN single crystals are reported for the first time.
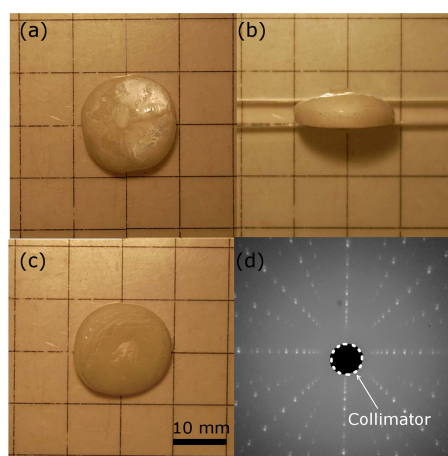
2 Experimental

2.1 Crystal growth

Crystal growth was carried out in a resistive heating furnace with a longitudinal thermal gradient smaller than 1 °C·cm^{-1}. KNLTN single crystals were grown by the TSSG method with [001]$_C$-oriented KTaO$_3$ seeds and an excess of Li$_2$O and K$_2$O acting as a self-flux. Three growth attempts, labeled as KNLTN1, KNLTN2 and KNLTN3, with increasing Ta^{5+} contents, were performed with a constant initial Li$^+$ content. Moreover, a pure (Na,K)NbO$_3$ (KNN0) single crystal has been grown as a reference with the same method. High purity powders of Na$_2$CO$_3$ (99.99 %, Aran Isles Chemical Inc.), Li$_2$CO$_3$ (99.99 %, Aran Isles Chemical Inc.), K$_2$CO$_3$ (99.99 %, Aran Isles Chemical Inc.,), Nb$_2$O$_5$ (99.99 %, Aran Isles Chemical Inc.,) and Ta$_2$O$_5$ (99.99 %, Aran Isles Chemical Inc.,) were used as the starting materials to synthesize KNLTN by high temperature solid-state reaction. After mixing for 24 h, the powders were kept at 800 °C for 24 h and finally melted at a temperature above 1200 °C. The batch was held at a soaking temperature about 20 °C above the saturation temperature for 24 h and subsequently the [001]$_C$-oriented KTaO$_3$ seed was immersed into the saturated liquid solution with a stirring rate of 40 rpm for 24 h under air atmosphere. The rotation speed was set in the range from 10 rpm to 35 rpm and the cooling rate was fixed between 0.1 °C·h^{-1} and 0.5 °C·h^{-1}.

2.2 Characterization

Chemical compositions were measured by combination of Electron Probe Micro Analysis (EPMA) and ICP-OES. Contents of each element, except Li$^+$, were first measured locally on polished single crystals by EPMA using a CAMECA SX-100 instrument operating at 20 keV and 20 nA. Complementary chemical analyses for all elements were performed by ICP-OES with a VARIAN 720-ES spectrometer. The solutions were prepared by dissolving 50 mg of crushed crystal in a 40 vol% HF solution at 180 °C with a 5-bar-autogenous pressure. ICP-OES and EPMA analysis results were averaged leading to a per-site-accuracy of 1 mol% for niobium and tantalum and 5 mol % for alkali elements, except lithium for which the accuracy is 0.24 mol%.

Powder X-ray diffraction (XRD) has been performed on crushed crystals using a PANalytical X'pert Pro MPD diffractometer with Cu K$_\alpha$ radiation and Bragg-Brentano geometry, while K$_{\alpha 2}$ reflections were removed after the measurement. Laue backscattering method was used to orientate single crystals. Backscattered diffraction patterns were collected using a CCD-camera device (Photonic Science dual lens coupled X-rays Laue system) after a 3–5 min stationary crystal irradiation with polychromatic X-rays supplied by a molybdenum anticathode. Raman spectra were carried out on single crystals by using a LabRAM HR800 Raman spectroscopy with the 633 nm radiation from a He-Ne laser at room temperature. Two sides of plate-like samples from all single crystals were covered with silver electrodes for electrical measurements. Temperature-dependent permittivity measurements have been carried out by a HP 4284A impedance analyzer with Nabertherm furnace in the temperature range between 30 °C and 450 °C and a Novocontrol Alpha-A high performance frequency analyzer in the temperature range from -100 °C to 30 °C. Electric-field-induced-strain curves and ferroelectric hysteresis loops were measured by a modified Sawyer-Tower setup with a 10 μF reference capacitance and an optical displacement sensor (Philtec, Inc.). Triangular electric field signals with a 10 Hz frequency were used.

Fig. 1 View from (a) the top, (b) the side and (c) the bottom; (d) backscattered Laue diffraction pattern of one of as-grown (Li,Na,K)(Nb,Ta)O$_3$ single crystals.

Table 2 Chemical compositions (EPMA, ICP-OES) and X-ray diffraction (XRD) structure of the as-grown KNLTN single crystals

	Element concentration C_s					Structure			
	A site			B site		Lattice parameters			
	Li (%)	Na (%)	K (%)	Nb (%)	Ta (%)	a (Å)	b (Å)	c (Å)	Phase
KNN0	0.0	11.9	88.1	100	0.0	3.963	5.681	5.707	O
KNLTN1	2.0	71.2	26.8	86.4	13.6	3.970	5.587	5.704	O
KNLTN2	2.0	62.6	35.4	80.8	19.2	3.984	3.984	4.127	T
KNLTN3	1.7	63.8	34.5	65.6	34.4	3.997	3.997	4.073	T

Table 3 Segregation coefficients with respect to the element concentrations in liquid solution $C_L(\infty)$

		Li	Na	K	Nb	Ta
KNN0	k_{eff}	/	2.38	0.93	1	/
KNN0	$C_L(\infty)$, (%)	0.00	5.00	95.00	100.00	0.00
KNLTN1	k_{eff}	0.18	3.31	0.40	0.89	4.69
KNLTN1	$C_L(\infty)$, (%)	11.38	21.54	67.08	97.10	2.90
KNLTN2	k_{eff}	0.13	3.90	0.52	0.85	3.84
KNLTN2	$C_L(\infty)$, (%)	15.30	16.05	68.65	95.00	5.00
KNLTN3	k_{eff}	0.11	3.98	0.89	0.82	1.72
KNLTN3	$C_L(\infty)$, (%)	15.30	16.05	68.65	80.00	20.00

3 Results and discussion

The KNLTN1 boule is depicted in Fig. 1 and looks overall milky. Fig. 1(d) provides the backscattered Laue diffraction pattern along [001]$_{PC}$ orientation. Typical size of the as-grown KNLTN crystals was about 20 mm in diameter and about 5 mm in thickness.

Chemical compositions of the as-grown crystals are listed in Table 2. The alkali contents of KNLTN crystals on the A-site are close to each other, making it possible to compare crystal properties as a function of Ta^{5+} content. The slight concentration difference can be ascribed to the small change of the compositions in the initial solutions and the difficulty in keeping the same crystal growth conditions during every growth process such as the volatilization rate of the liquid solution with respect to the growth time.[21]

The difference between the crystal composition and the concentration of the elements in the initial liquid solution can be described by the classical effective segregation coefficient k_{eff}:[20]

$$k_{eff} = \frac{1}{1+\left(\frac{1}{k_0}-1\right)\exp\left(\frac{-v\delta}{D}\right)} \times \frac{1}{k_{volatilization}} \qquad (1)$$

where k_0 is the thermodynamic segregation coefficient, $k_{volatilization} \geq 1$ is defined as the volatilization contribution factor to the effective segregation coefficient, v is the growth rate, δ is the thickness of the solid-liquid boundary layer and D is the diffusion coefficient of the element in the liquid solution.

In the case of flux growth, the growth rate is very slow so v is considered to be close to zero. According to the fact that the volatilization of the solution during the growth process acts as an important factor on the effective segregation coefficients with respect to the growth time, the effective segregation coefficient is assumed as:

$$k_{eff} \approx \frac{k_0}{k_{volatilization}} \qquad (2)$$

Moreover, it is assumed that the equilibrium phases were reached during the flux growth process. At equilibrium state, no composition gradient can be detected in every phase. It is therefore assumed that both solid and liquid phases were uniform. Hence, the effective segregation coefficient k_{eff} can also be expressed as equation (3), arising from the well-known Scheil's equation.[20]

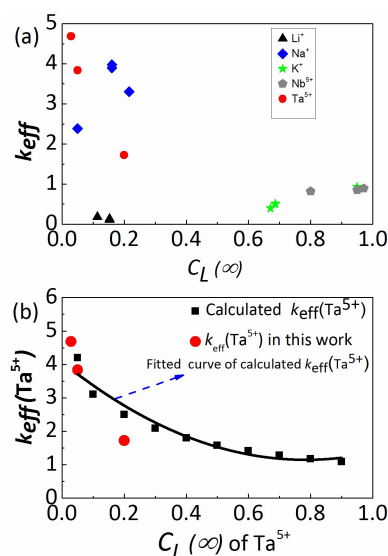$$k_{eff} = \frac{C_S}{C_L(\infty)} \qquad (3)$$

where where C_S is the concentration of the element in the solid

phase, i.e. in the single crystal, and $C_L(\infty)$ the concentration of the element in the liquid solution at the beginning of crystal growth.

Table 3 and Fig. 2(a) displays k_{eff} of individual elements as a function of $C_L(\infty)$ for the four crystal growth attempts. Effective segregation coefficients $k_{eff}(Li^+)$, $k_{eff}(K^+)$ and $k_{eff}(Nb^{5+})$ are lower than 1, while $k_{eff}(Na^+)$ and $k_{eff}(Ta^{5+})$ are higher than 1. Moreover, increasing concentration of K$^+$ and Nb^{5+} ions in the initial liquid solutions resulted in increasing k_{eff}, while the opposite trend is observed for Ta^{5+} ions. This trend is directly related to the slope signs of the liquidus and solidus lines, as described by analogy in KNbO$_3$-KTaO$_3$ and NaNbO$_3$-KNbO$_3$ phase diagrams where two ions on A or B site were considered.[30, 31] From the KNbO$_3$-KTaO$_3$ phase diagram[30], a positive slope of the liquidus curve induces $k_{eff}(Ta^{5+})$>1. In addition, Fig. 2(b) shows the calculated $k_{eff}(Ta^{5+})$ in the crystal decreases with increasing the Ta^{5+} content in the liquid. $k_{eff}(Ta^{5+})$ values of the present work are consistent with those calculated from the phase diagram, as presented in Fig. 2(b). In addition, it can
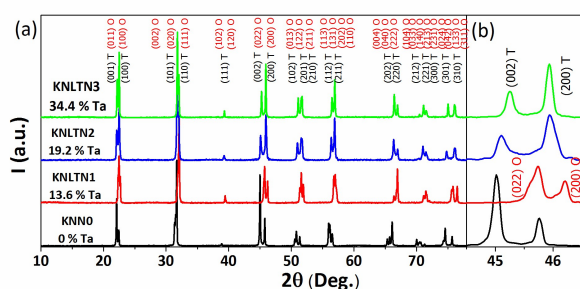

Fig. 2 (a) Effective segregation coefficient k_{eff} of individual elements as a function of the concentration of the elements in the liquid solution $C_L(\infty)$, and (b) k_{eff} of tantalum as a function of Ta molar concentrations in the liquid solution compared with that deduced from the pseudo-binary KNbO$_3$-KTaO$_3$ phase diagram given by Reisman *et al.*[30].

be inferred that $k_{eff}(Ta^{5+})>1$ leads to a strong depletion of Ta^{5+} in the liquid solution and subsequently to a step by step decrease of its incorporation into the crystal as the growth proceeds. Using the same approach, the negative slope of the liquidus curve in the $NaNbO_3$-$KNbO_3$ system[31] leads to a reverse behaviour for K^+: $k_{eff}(K^+)<1$ and an increasing potassium content along the growth direction. Changes of Ta^{5+} and K^+ concentrations should be detected in principle along the growth directions of all crystals, and it therefore should affect their electrical properties due to compositional inhomogeneity. However, due to the small sample size, the concentration of elements has been considered as homogeneous for further electrical characterization.

Besides, the k_{eff} values of lithium measured in the KNLTN crystals were found to be about 0.13, which is consistent with the previous work of Hofmeister et $al.$,[32] where $k_{eff}(Li^+)$ in $(Li_yK_{1-y})(Nb_{0.65}Ta_{0.35})O_3$: Cu crystals was calculated to be approximately 0.125. Higher Li^+ content could lead to the formation of a secondary tetragonal-tungsten-bronze-type phase because of its limited solubility in KNN matrix, as previously reported in polycrystalline ceramics.[33, 34] Therefore, the Li^+ contents in KNLTN single crystals are low and almost constant. Moreover, according to the work of Sadel et $al.$,[35] the $k_{eff}(Li^+)$ in $(Li_{0.02}Na_{0.98})NbO_3$ (LNN) crystals grown with $NaBO_2$ flux at 1147°C was calculated to be 0.25. The higher value, as compared to the present work, highlights the influence of volatilization of lithium-based compounds on its effective segregation. Note that substantial evaporation of lithium from the solution is reported to start at 1197 °C, which is in the working temperature range of KNLTN crystal growth. In the present work, compared with Sadel's et $al.$ work where the volatilization contribution of lithium is not so significant that $k_{eff} = k_0$ for LNN, we assume that the same thermodynamic segregation coefficient k_0 should be obtained for KNLTN due to the low lithium solubility in the perovskite matrix and the close lithium concentrations in the initial solution. Hence, $k_{volatilization}$ factor was estimated to be in the range from 1.39 to 2.27 for KNLTN.

Finally, it is worth mentioning that segregation trends of alkali elements in KNLTN are similar regardless whether two or three different ions are present on the A-site: $k_{eff}(Li^+)<1$, $k_{eff}(K^+)<1$ and $k_{eff}(Na^+)>1$. However, we note that $k_{eff}(Na^+)$ depends on the presence or the absence of lithium in the initial composition containing potassium. As evident, $k_{eff}(Na^+)$ should decrease monotonically with increasing concentration of Na^+ in the liquid solution.[31] In the present work, the initial content of sodium in

KNN0 is 5% and $k_{eff}(Na^+)=2.38$. Compared with the previous work of Reisman et $al.$[31], the $k_{eff}(Na^+)$ value is higher than 1 as expected. Nevertheless, $k_{eff}(Na^+)$ in KNN0 single crystal should be higher than those of KNLTN2 ($k_{eff}(Na^+)=3.90$) and KNLTN3 ($k_{eff}(Na^+)=3.98$) where the initial content of sodium is 16.05%. The lower $k_{eff}(Na^+)$ in KNN0 single crystal suggests a stronger competition between the three alkali elements regarding their incorporation into the A-site, as compared to the previous literature reports where only two ions were introduced into A or B sites.[30, 31] It appears that the presence of lithium increases $k_{eff}(Na^+)$ in KNLNT crystals, as compared to systems without lithium.

XRD patterns obtained on crushed single crystals are presented in Fig. 3(a), while the calculated lattice parameters and the crystallographic structure are provided in Table 2. The reason for different room temperature structures of KNLTN single crystals is the variation of the Ta^{5+} content. All samples are single phase with the perovskite structure and no secondary phase is observed. In order to emphasize the details of the crystal structure, the peaks of the 2θ region around 45° are enlarged in Fig. 3(b). The ratio of intensities I_{022}/I_{200} for the KNN0 and KNLTN1 samples are close to 2, while for KNLTN2 and KNLTN3 the I_{002}/I_{200} values are about 0.5. These ratios confirm that the phase evolves from orthorhombic to tetragonal with increasing the Ta^{5+} content. This phenomenon was induced by the substitution of Nb^{5+} (R=0.069 nm; CN6) ions by the slightly smaller Ta^{5+} (R=0.068 nm; CN6)[36] as previously reported for Ta^{5+}-modified KNN-based polycrystalline ceramics.[37, 38]

Fig. 4 shows the Raman spectra of $[001]_{PC}$-oriented KNLTN single crystals. The BO_6 octahedron of the KNLTN system has six vibrational modes $1A_{1g}(v_1)+1E_g(v_2)+2F_{1u}(v_3,v_4)+F_{2g}(v_5)+F_{2u}(v_6)$, where $1A_{1g}(v_1)+1E_g(v_2)+F_{1u}(v_3)$ are stretching modes and others are bending modes.[39] The Raman peaks between 100 cm^{-1} to 200 cm^{-1} correspond to translational modes of A-site cations and the rotations of the BO_6 octahedron. The modes in the range from 200 cm^{-1} to 1000 cm^{-1} come from the stretching and bending vibrations of the BO_6 octahedron.[39, 40] With increasing Ta^{5+} content, v_2 modes and the shoulders of v_5 modes become weaker, indicating a phase transition from the orthorhombic to the tetragonal phase. On the other hand, the pure KNN single crystal possesses a weaker v_1 and
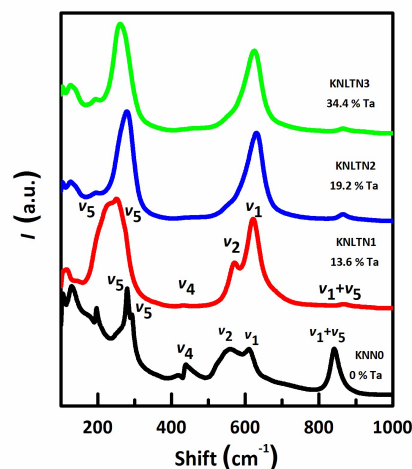

Fig. 3 XRD patterns of the crushed KNLTN single crystals. (a) Full range and (b) enlarged region of $(002)_T/(200)_T$ or $(022)_O/(200)_O$ peaks.
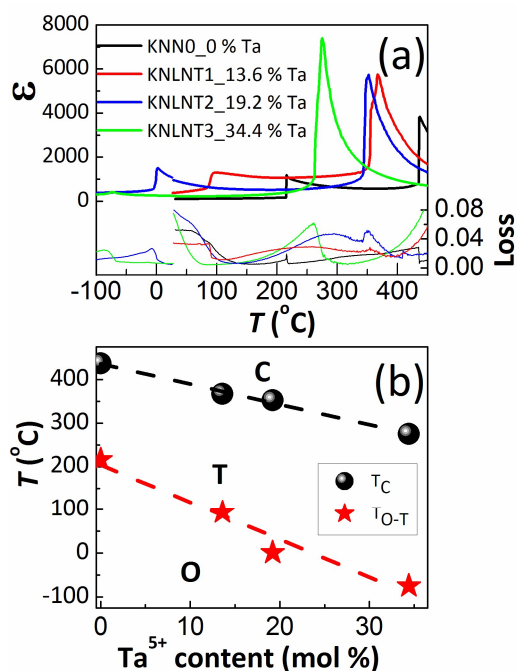

Fig. 4 Raman spectra of $[001]_{PC}$-oriented KNLTN single crystals with various Ta^{5+} contents at room temperature.

Fig. 5 (a) Temperature-dependent dielectric permittivity and losses of $[001]_{PC}$-oriented KNLTN single crystals during heating from -100 ^{o}C to 450 ^{o}C (10 kHz), and (b) phase transition temperatures (T_c and T_{O-T}) as a function of Ta^{5+} content. The minor discontinuity at 30 °C is related to the use of different measurement setups for the low and high temperature range.
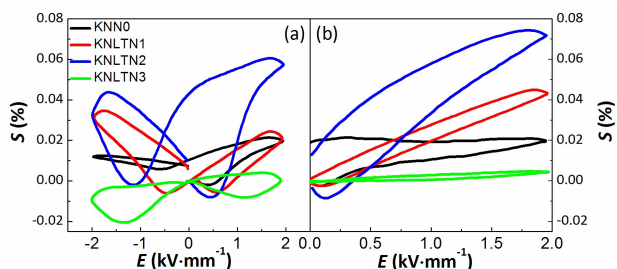
v_5 mode, but a stronger v_5+v_1 coupling mode and v_4 mode, as compared to KNLTN single crystals. The decoupling effect of v_1 and v_5 modes might result from the weaker interactions among the BO_6 octahedra after Li^+ and Ta^{5+} substitutions.

Fig. 5(a) provides the temperature-dependent dielectric permittivity and losses of $[001]_{PC}$-oriented KNLTN single crystals at 10 kHz in the temperature range from -100 ^{o}C to 450 ^{o}C. Fig. 5(b) displays the phase transition temperatures with various Ta^{5+} contents, obtained from the dielectric measurements. The increase of Ta^{5+} content shifts both T_C and T_{O-T} to lower temperatures and the decrease could be fitted with linear equations (4) and (5):

$$T_C(°C) = -(4.6 \pm 0.23) \cdot x \ (mol\%) + (436 \pm 4,7) \quad (4)$$

$$T_{O-T}(°C) = -(8.6 \pm 1.25) \cdot x \ (mol\%) + (204 \pm 26.19) \quad (5)$$

where x is the Ta^{5+} mol% content. The rates of decrease for T_C and

Fig. 6 Electric-field-induced (a) bipolar and (b) unipolar strains of $[001]_{PC}$-oriented KNLTN single crystals under 2 kV·mm^{-1} and 10 Hz.

T_{O-T} are 4.6 ^{o}C/mol%Ta and 8.6 ^{o}C/mol%Ta, respectively. The shift of the phase transitions is attributed to the different electronegativity[9] between Ta^{5+} and Nb^{5+} and the change of the Goldschmidt tolerance factor t.[41] The latter can be expressed as,

$$t = \frac{(R_A + R_O)}{\sqrt{2}(R_B + R_O)} \quad (6)$$

where R_A, R_B and R_O are the ionic radii of the corresponding perovskite sites. The tolerance factor decreases slightly after more B sites are occupied by the smaller Ta^{5+} and therefore the degree of lattice distortion is reduced with increasing Ta^{5+} content. Lower electronegativity of Ta^{5+} also weakens the B-O bond and therefore the ability of off-center movements of B-site ions during the cubic-tetragonal phase transition is decreased.

The influence of the K/Na ratio on the phase structure and electrical properties in polycrystalline $(K,Na)NbO_3$ ceramics was previously discussed by Zhang *et al.*.[42] By changing the K/Na ratio from 70/30 to 30/70, both phase transition temperatures T_C and T_{O-T} decreased by less than 10 ^{o}C. Similar results were also obtained by others.[43, 44] It can therefore be concluded that the observed changes in T_C and T_{O-T} are predominantly related to the Ta^{5+} content and the influence of the K/Na ratio can be neglected. The relative dielectric permittivities $\varepsilon_r/\varepsilon_0$ of KNN0, KNLTN1, KNLTN2 and KNLTN3 at 30 ^{o}C are 107, 371, 964 and 231, respectively (Fig. 5(a)). KNLTN2 with 19.2 % Ta^{5+} displays the highest dielectric permittivity at room temperature. Note also that this value is higher than the values from most other literature reports (see Table 1).

Fig. 6 (a) depicts the bipolar electric-field-induced strain curves (S-E) of $[001]_{PC}$-oriented KNLTN single crystals. All samples exhibit typical butterfly-shaped S-E loops with evident negative strain (S_{neg}).[5, 45] The unipolar strain curves are depicted in Fig. 6(b). KNLTN2 presents the highest bipolar and unipolar strains at the maximum investigated E-field of 2 kV·mm^{-1}. This is due to the proximity of its T_{O-T} to the room temperature, whereby the energy barrier for polarization rotation decreases, leading to increased strain values.

The electric field corresponding to the largest absolute value in S_{neg} was taken as coercive field E_C.[46, 47] The asymmetry in the strain curves in Fig. 6(a) can be explained by the existence of an internal bias field E_i. The measured internal bias fields are approximately 20 % of the corresponding coercive fields, as shown in Fig. 7(a). Although the origin of the internal bias fields in these samples is not clear, it might originate from the defect dipoles present in the as-grown single crystals. It is expected that A-site elements K^+, Na^+, and Li^+ evaporate from the crystal during the high-temperature growth process, creating V_A' vacancies.[48] As a consequence, oxygen vacancies $V_O^{··}$ were also created during the perovskite formation due to charge compensation. This could lead to the formation of $(V_A'-V_O^{··})^·$ defect dipoles,[49] which might be responsible for the observed internal bias field and the asymmetry of the bipolar S-E loops.

Coercive field E_C and internal field E_i were calculated by Equations (7) and (8) and are provided in Fig. 7(a).

$$E_C = \frac{|E_C^+|}{2} + \frac{|E_C^-|}{2} \quad (7)$$

ARTICLE

Journal Name

$$E_i = |\frac{|E_C^+|}{2} - \frac{|E_C^-|}{2}|$$ (8)

where E_C^+ and E_C^- represent the positive and negative coercive fields, respectively.

In Fig. 6(a), the maximum positive strain S_{pos} of $[001]_{PC}$-oriented KNLTN crystals was 0.06 % when Ta^{5+} content reached 19.2 %. However, further increasing the Ta^{5+} content up to 34.4 % leads to a significant decrease of S_{pos}. KNLTN3 with 34.4 % Ta^{5+} has a much larger absolute S_{neg} value compared to its S_{pos} value. This phenomenon was previously observed in $0.62Pb(Mg_{1/3}Nb_{2/3})O_3$-$0.38PbTiO_3$ (PMN-PT) single crystals.[46] It has been explained that the depolarization field and internal stresses are too small to produce significant back switching of polarization in the absence of grain boundaries. However, studies of lead-based single crystals revealed that the shape of the bipolar strain curves depends on the crystallographic orientation and phase structure.[50]

Fig. 7(a) shows that the E_C of KNLTN3 is more than 2 times higher than those of other crystals with lower Ta^{5+} contents. Increasing the Ta^{5+} content leads to a remarkable increase of E_c due to the presence of the tetragonal phase. The large-signal converse piezoelectric constants d_{33}^* of $[001]_{PC}$-oriented KNLTN single crystals is depicted in Fig. 7(b). The d_{33}^* values of KNN0, KNLTN1, KNLTN2 and KNLTN3 measured at 2 $kV\cdot mm^{-1}$ are 102, 221, 368 and 22 $pm\cdot V^{-1}$, respectively. KNLTN2 crystal has the highest d_{33}^* value due to the proximity of the T_{O-T} to room temperature.

Fig. 8 displays the ferroelectric hysteresis loop of $[001]_{PC}$-oriented KNLTN2 single crystal measured at 2 $kV\cdot mm^{-1}$ and 10 Hz. The remanent polarization is approximately 5 $\mu C\cdot cm^{-2}$ and the coercive field is 0.80 $kV\cdot mm^{-1}$, which is in agreement with the value 0.76 $kV\cdot mm^{-1}$ obtained from the bipolar strain loop. Unfortunately the ferroelectric loops of other crystals could not be measured due to the high leakage currents. Piezoelectric, ferroelectric and dielectric parameters of all $[001]_{PC}$-oriented KNLTN single crystals with different Ta^{5+} contents are summarized in Table 4.

Conclusions

Li^+-, Ta^{5+}-modified KNN single crystals were grown by the TSSG method and centimeter-sized boules were successfully obtained. The effective segregation coefficients with respect to the initial concentrations of individual elements in the liquid were studied. Whereas Ta^{5+} and Nb^{5+} concentrations measured in the single crystals are consistent with literature, alkali elements (Li^+, Na^+ and K^+) are strongly dependent on each other regarding their incorporation into the lattice as well as the volatilization of the solution during the growth, particularly for Li^+. XRD and Raman measurements determine the transition from the orthorhombic to the tetragonal phase with increasing Ta^{5+} content. A linear decrease of the phase transition temperatures (T_C and T_{O-T}) was found with increasing the Ta^{5+} content. The highest strain and large-signal piezoelectric coefficient of 368 $pm\cdot V^{-1}$ were observed in the $[001]_{PC}$-oriented single crystal with 19.2 % Ta^{5+}, which was ascribed to the proximity of the T_{O-T} to room temperature. In addition, the observed internal fields might be related to the presence of $(V_A'\text{-}V_O^{¨})^·$ defect dipoles created during the high-temperature crystal growth, and were found to contribute to the asymmetry of
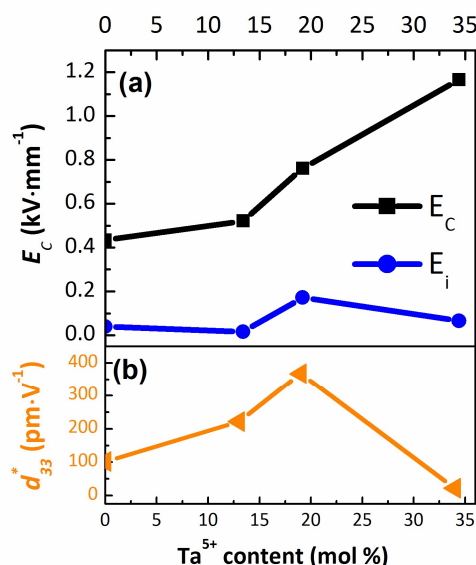

Fig. 7 (a) E_C, E_i, and (b) piezoelectric constant d_{33}^* at 2 $kV\cdot mm^{-1}$ of the $[001]_{PC}$-oriented KNLTN single crystals with different Ta^{5+} contents.

bipolar strain curves.

Acknowledgements

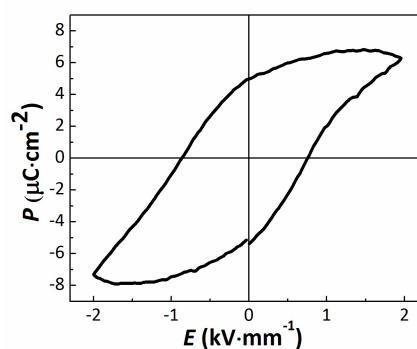**Fig. 8** Ferroelectric hysteresis loop of $[001]_{PC}$-oriented KNLTN2 single crystal under 2 $kV\cdot mm^{-1}$ and 10 Hz.

CrystEngComm Accepted Manuscript

Table 4 Piezoelectric, ferroelectric and dielectric parameters of $[001]_{PC}$ oriented KNLTN single crystals with different Ta^{5+} contents

SAMPLE (Ta^{5+} mol%)	d_{33}^* (pm·V^{-1})	S_{pos} (%), Bi^a	$-S_{neg}$ (%), Bi^a	S_{max} (%), Uni^b	E_C (kV·mm^{-1})	E_i (kV·mm^{-1})	ε_r (RT)	ε_{max} (T_C)	T_{O-T} (°C)	T_C (°C)
KNN0 (0)	102	0.020	0.002	0.020	0.44	0.040	107	3814	216	437
KNLTN1 (13.4)	221	0.024	0.005	0.044	0.52	0.017	371	5765	94	367
KNLTN2 (19.2)	368	0.060	0.008	0.074	0.76	0.172	964	5743	1	352
KNLTN3 (34.4)	22	0.004	0.008	0.004	1.17	0.065	231	7394	-75	275

^{a} Obtained from bipolar strain curves.
^{b} Obtained from unipolar strain curves.

References

1. J. Rödel, W. Jo, K. T. Seifert, E. M. Anton, T. Granzow and D. Damjanovic, *J. Am. Ceram. Soc.*, 2009, **92**, 1153-1177.
2. J. F. Li, K. Wang, F. Y. Zhu, L. Q. Cheng and F. Z. Yao, *J. Am. Ceram. Soc.*, 2013, **96**, 3677-3696.
3. T. R. Shrout and S. J. Zhang, *J. Electroceram.*, 2007, **19**, 113-126.
4. T. Takenaka, K.-i. Maruyama and K. Sakata, *Jpn. J. Appl. Phys.*, 1991, **30**, 2236.
5. W. Jo, R. Dittmer, M. Acosta, J. Zang, C. Groh, E. Sapper, K. Wang and J. Rödel, *J. Electroceram.*, 2012, **29**, 71-93.
6. W. Liu and X. Ren, *Phys. Rev. Lett.*, 2009, **103**, 257602.
7. H. Liu, Q. Li, Y. Li, N. Luo, J. Shim, J. Gao, Q. Yan, Y. Zhang and X. Chu, *J. Am. Ceram. Soc.*, 2014, **97**, 2076-2081.
8. D. R. Brandt, M. Acosta, J. Koruza and K. G. Webber, *J. Appl. Phys.*, 2014, **115**, 204107.
9. Y. Saito, H. Takao, T. Tani, T. Nonoyama, K. Takatori, T. Homma, T. Nagaya and M. Nakamura, *Nature*, 2004, **432**, 84-87.
10. J. Wu, D. Xiao and J. Zhu, *Chem. Rev.*, 2015, **115**, 2559-2595.
11. Y. F. Chang, Z. P. Yang, D. F. Ma, Z. H. Liu and Z. L. Wang, *J. Appl. Phys.*, 2009, **105**, 054101.
12. S. J. Zhang, R. Xia and T. R. Shrout, *Appl. Phys. Lett.*, 2007, **91**, 132913.
13. Z. Y. Shen, K. Wang and J. F. Li, *Appl. Phys. A*, 2009, **97**, 911-917.
14. E. K. Akdoğan, K. Kerman, M. Abazari and A. Safari, *Appl. Phys. Lett.*, 2008, **92**, 112908.
15. Y. Saito and H. Takao, *Ferroelectrics*, 2006, **338**, 17-32.
16. S. J. Zhang and F. Li, *J. Appl. Phys.*, 2012, **111**, 031301.
17. X. Huo, R. Zhang, L. Zheng, S. Zhang, R. Wang, J. Wang, S. Sang, B. Yang and W. Cao, *J. Am. Ceram. Soc.*, 2015, **98**, 1829-1835.
18. H. Uršič, A. Benčan, M. Škarabot, M. Godec and M. Kosec, *J. Appl. Phys.*, 2010, **107**, 033705.
19. H. Tian, C. Hu, X. Meng, P. Tan, Z. Zhou, J. Li and B. Yang, *Cryst. Growth Des.*, 2015, **15**, 1180-1185.
20. K. A. Jackson, *Kinetic Processes: Crystal Growth, Diffusion, and Phase Transformations in Materials*, Wiley, New York, 2004.
21. M. Prakasam, P. Veber, O. Viraphong, L. Etienne, M. Lahaye, S. Pechev, E. Lebraud, K. Shimamura and M. Maglione, *C. R. Phys.*, 2013, **14**, 133-140.
22. X. Huo, L. Zheng, R. Zhang, R. Wang, J. Wang, S. Sang, Y. Wang, B. Yang and W. Cao, *CrystEngComm*, 2014, **16**, 9828-9833.
23. X. Q. Huo, L. M. Zheng, S. J. Zhang, R. Zhang, G. Liu, R. Wang, B. Yang, W. W. Cao and T. R. Shrout, *Phys. Status Solidi RRL*, 2014, **8**, 86-90.
24. L. M. Zheng, X. Q. Huo, R. Wang, J. J. Wang, W. H. Jiang and W. W. Cao, *CrystEngComm*, 2013, **15**, 7718-7722.
25. L. M. Zheng, J. J. Wang, X. Q. Huo, R. Wang, S. J. Sang, S. Y. Li, P. Zheng and W. W. Cao, *J. Appl. Phys.*, 2014, **116**, 044105.
26. M. Bah, F. Giovannelli, R. Retoux, J. Bustillo, E. L. Clezio and I. Monot-Laffez, *Cryst. Growth Des.*, 2016, **16**, 315-324.
27. Y. Liu, G. Xu, J. Liu, D. Yang and X. Chen, *J. Alloys Compd.*, 2014, **603**, 95-99.
28. K. Chen, G. S. Xu, D. F. Yang, X. F. Wang and J. B. Li, *J. Appl. Phys.*, 2007, **101**, 044103.
29. H. Deng, X. Y. Zhao, H. W. Zhang, C. Chen, X. B. Li, D. Lin, B. Ren, J. Jiao and H. S. Luo, *CrystEngComm*, 2014, **16**, 2760-2765.
30. A. Reisman, S. Triebwasser and F. Holtzberg, *J. Am. Chem. Soc.*, 1955, **77**, 4228-4230.
31. A. Reisman and E. Banks, *J. Am. Chem. Soc.*, 1958, **80**, 1877-1882.
32. R. Hofmeister, A. Yariv and A. Agranat, *J. Cryst. Growth*, 1993, **131**, 486-494.
33. Y. Guo, K.-i. Kakimoto and H. Ohsato, *Appl. Phys. Lett.*, 2004, **85**, 4121-4123.
34. N. Klein, E. Hollenstein, D. Damjanovic, H. J. Trodahl, N. Setter and M. Kuball, *J. Appl. Phys.*, 2007, **102**, 014112-014112-014118.
35. A. Sadel, R. Von der Mühll, J. Ravez, J. Chaminade and P. Hagenmuller, *Solid State Commun.*, 1982, **44**, 345-349.
36. G. E. McGuire, G. K. Schweitzer and T. A. Carlson, *Inorg. Chem.*, 1973, **12**, 2450-2453.
37. Y. Chang, Z.-p. Yang, D. Ma, Z. Liu and Z. Wang, *J. Appl. Phys.*, 2008, **104**, 024109.
38. Z. P. Yang, Y. F. Chang and L. L. Wei, *Appl. Phys. Lett.*, 2007, **90**, 042911.
39. K. i. Kakimoto, K. Akao, Y. Guo and H. Ohsato, *Jpn. J. Appl. Phys.*, 2005, **44**, 7064.
40. S. Sang, Z. Yuan, L. Zheng, E. Sun, R. Zhang, J. Wang, R. Wang, B. Yang and M. Liu, *Optical Materials*, 2015, **45**, 104-108.
41. V. M. Goldschmidt, *Naturwissenschaften*, 1926, **14**, 477-485.
42. Q. Zhang, B. Zhang, H. Li and P. Shang, *Rare Metals*, 2010, **29**, 220-225.
43. W. Jiagang, X. Dingquan, Z. Jianguo, Y. Ping and W. Yuanyu, *J. Appl. Phys.*, 2008, **103**, 024102.
44. L. Wu, J. Zhang, C. Wang and J. Li, *J. Appl. Phys.*, 2008, **103**, 4116.

45. J. Fu, R. Z. Zuo, H. Qi, C. Zhang, J. F. Li and L. T. Li, *Appl. Phys. Lett.*, 2014, **105**, 242903.
46. G. Viola, T. Saunders, X. Wei, K. B. Chong, H. Luo, M. J. Reece and H. Yan, *J. Adv. Dielectr.*, 2013, **03**, 1350007.
47. A. Achuthan and C. T. Sun, *Acta Mater.*, 2009, **57**, 3868-3875.
48. A. Popovič, L. Bencze, J. Koruza and B. Malič, *RSC Advances*, 2015, **5**, 76249-76256.
49. R.-A. Eichel, *J. Electroceram.*, 2007, **19**, 11-23.
50. S.-E. Park and T. R. Shrout, *J. Appl. Phys.*, 1997, **82**.